Journal of Oceanography, Vol. 63, pp. 897 to 911, 2007

Assessing the West Ridge of Luzon Strait as an Internal Wave Mediator

Shenn-Yu Chao[1]*, Dong-Shan Ko[2], Ren-Chieh Lien[3] and Ping-Tung Shaw[4]

[1]*Horn Point Laboratory, University of Maryland Center for Environmental Science, Cambridge, MD 21613-0775, U.S.A.*
[2]*Naval Research Laboratory, Stennis Space Center, MS 39529, U.S.A.*
[3]*Applied Physics Laboratory, University of Washington, Seattle, WA 98105, U.S.A.*
[4]*Department of Marine, Earth and Atmospheric Sciences, North Carolina State University, Raleigh, NC 27695-8208, U.S.A.*

(Received 26 July 2006; in revised form 28 May 2007; accepted 29 May 2007)

The Luzon Strait is blocked by two meridional ridges at depths, with the east ridge somewhat higher than the west ridge in the middle reaches of the Strait. Previous numerical models identified the Luzon Strait as the primary generation site of internal M_2 tides entering the northern South China Sea (Niwa and Hibiya, 2004), but the role of the west-versus-east ridge was uncertain. We used a hydrostatic model for the northern South China Sea and a nonhydrostatic, process-oriented model to evaluate how the west ridge of Luzon Strait modifies westward propagation of internal tides, internal bores and internal solitary waves. The dynamic role of the west ridge depends strongly on the characteristics of internal waves and is spatially inhomogeneous. For M_2 tides, both models identify the west ridge in the middle reaches of Luzon Strait as a dampener of incoming internal waves from the east ridge. In the northern Luzon Strait, the west ridge is quite imposing in height and becomes a secondary generation site for M_2 internal tides. If the incoming wave is an internal tide, previous models suggested that wave attenuation depends crucially on how supercritical the west ridge slope is. If the incoming wave is an internal bore or internal solitary wave, our investigation suggests a loss of sensitivity to the supercritical slope for internal tides, leaving ridge height as the dominant factor regulating the wave attenuation. Mechanisms responsible for the ridge-induced attenuation are discussed.

Keywords:
· Luzon Strait,
· South China Sea,
· internal solitary waves,
· internal tides.

1. Introduction

The Luzon Strait, which is a passage from the western Pacific to the South China Sea, is blocked by two ridges at depths (Fig. 1). For the most part, the east ridge is higher than the west ridge (rectangular area in Fig. 1) except in areas off southern Taiwan, where the west ridge meets the continental shelf. Figure 1(a) also shows the depth-integrated M_2 internal tidal energy flux predicted by the three-dimensional tidal model of Niwa and Hibiya (2004). Zonal divergence of this energy flux, indicative of internal tide generation, suggested two generation sites for the internal M_2 tide. The primary source of M_2 internal tides entering the northern South China Sea appears to originate from the east ridge, propagate over the deeper (central) reaches of the west ridge and thereafter progress to the west-northwest, presumably caused by bottom steering. In northern reaches of the Luzon Strait (>21°N), the east ridge does not appear to generate energetic internal tides as the internal energy flux shows little divergence over it (Fig. 1(a)). Instead, the northern, shallow portion of the west ridge shows modest zonal divergence of internal tide energy flux (Fig. 1(a)) and therefore appears to be a secondary source of M_2 internal tides for the northern South China Sea.

Conceivably, energetic internal tides lead to ubiquity of internal solitary waves in the northern South China Sea (Lynch *et al.*, 2004). Figure 2, reproduced from Zhao *et al.* (2004), shows a composite of internal solitary waves derived from satellite images from 1995 to 2001. These waves appear to the west of the west ridge. Excluding the continental shelf and slope region in the far west, they are mostly single waves (dashed lines in Fig. 2). Occa-

* Corresponding author. E-mail: chao@hpl.umces.edu

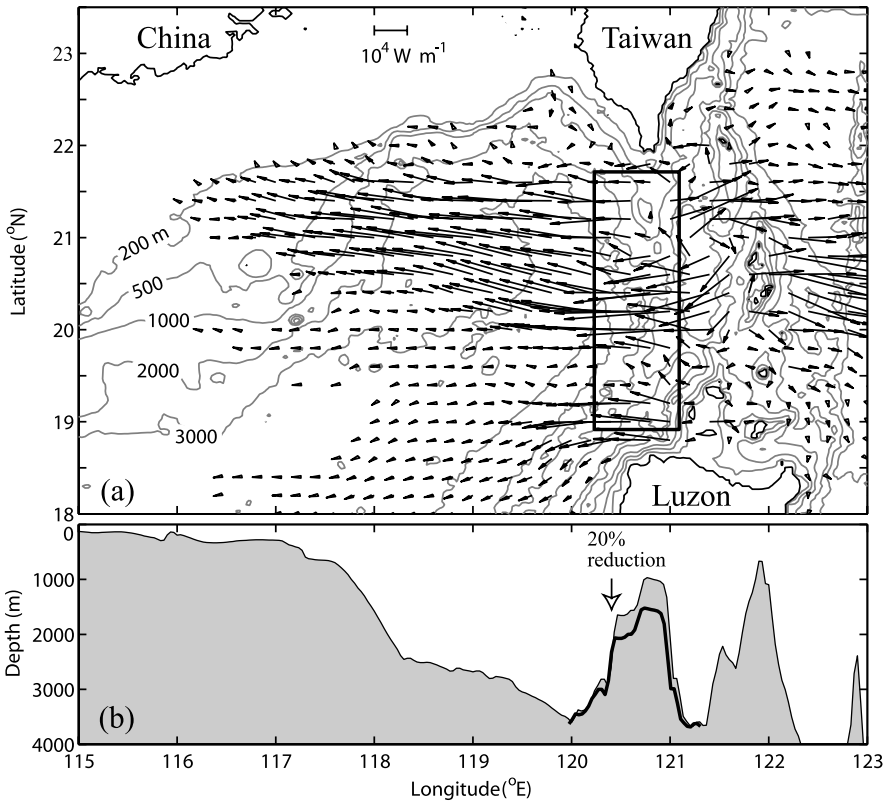

Fig. 1. (a) Bathymetry of northern South China Sea and model-predicted distribution of depth-integrated M_2 baroclinic energy flux by Niwa and Hibiya (2004). The rectangle delineates the deeper portion of the west ridge in the Luzon Strait; ridge height in this portion will be reduced by 20% in a numerical experiment below. (b) Zonal section of bottom topography at 21°N with the thick line showing 20% reduction of the west ridge height.

sional packets of multiple waves (solid lines) also appeared to the immediate west of the west ridge. Over the continental shelf and upper continental slope in the far west (west of 118°E), these waves become packets of multiple waves; shoaling bottom topography could conceivably lead to the transformation.

A brief preview of internal solitary wave generation helps put the forthcoming numerical results in perspective. Figure 3 illustrates, to lowest order, how a tall ridge such as the east ridge of the Luzon Strait transforms barotropic tides into internal solitary waves. The ridge first converts barotropic tides to internal tides propagating westward (Fig. 3(a)). Because the wave trough propagates faster than the surrounding portion, the continuous wave steepening transforms the internal tide to an internal bore (Fig. 3(b)). The internal bore will evolve into an internal solitary wave at a distance (L) away from the ridge (Fig. 3(c)). If the ridge is sufficiently tall or the tide is sufficiently strong, the solitary wave will further develop into a packet of rank-ordered internal solitary waves (Fig. 3(d)). Otherwise the solitary wave will remain as a single wave as it continues its westward track before moving onto the shoaling continental slope and shelf. The entire transformation process also shortens the wavelength continuously.

The distance between the ridge and first appearance of the internal solitary wave (L in Fig. 3(c)) depends on the tidal strength, ridge height and tidal frequency. For strong tides or tall ridges, L can be as short as a few tens of kilometers. For weaker tides or milder ridge heights, L can increase to a few hundreds of kilometers. The distance also depends on the tidal frequency. The wavelength of a diurnal internal tide is about twice as long as that of a semidiurnal internal tide. Transformation from internal tide to internal bore through nonlinear wave steepening requires the wave trough to move from the center of a moving wavelength to the forefront. Roughly speaking, diurnal internal tides will have to travel twice as far as semidiurnal counterparts to complete the transformation, and the zonal extent of the northern South China Sea may not be wide enough to allow for the complete transformation. Thus, in terms of the occurrence of internal solitary waves, the theoretical expectation favors the transformation from semidiurnal internal tides. In the north-

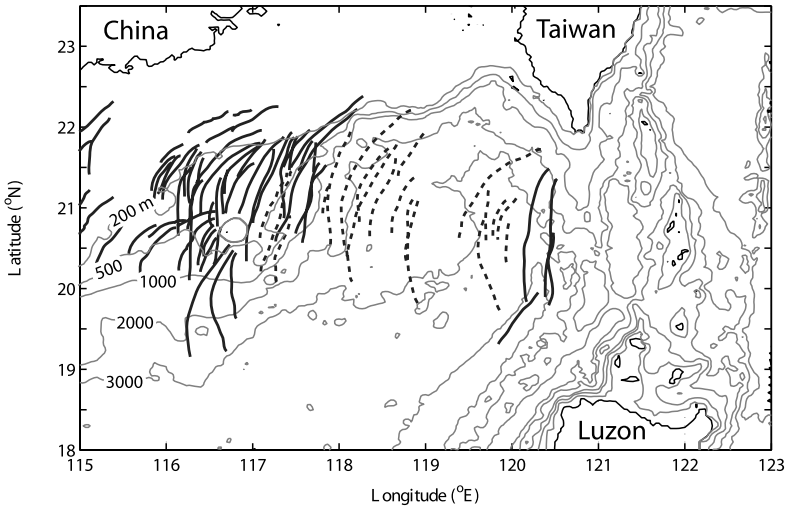

Fig. 2. Composite (1995–2001) satellite image of internal solitary waves in the northern South China Sea (adopted from Zhao *et al*., 2004). Dashed and solid lines indicate surface signatures of single waves and packets of multiple waves, respectively.

ern South China Sea, however, the semidiurnal internal tide contains a strong diurnal beat (Yang *et al*., 2004; Liu *et al*., 2006). The interaction between the two tidal constituents should be responsible for the diurnal beat, but is beyond the scope of this work.

Beyond the first order depiction of Fig. 3, the west ridge adds further complexities. First and foremost, the west ridge may help "lock" the Kuroshio front in place. Figure 4, derived from a hydrostatic model to be described in Section 2, shows the mesoscale circulation in and around the Luzon Strait at 150 m depth (Fig. 4(a)) and a zonal section of meridional currents and temperature at 21°N (Fig. 4(b)) on April 28, 2005. The Kuroshio encroachment is evident. At 21°N, the Kuroshio Current is centered over the west ridge with a depth scale of about 700 m (Fig. 4(b)). Isotherms (white curves) rise westward in support of the northward current. Rising isotherms decrease the phase speed of internal waves with distance westward. In consequence, westward propagating internal waves may decelerate, amplify, and even transform into internal solitary waves without the aid of other triggers such as a ridge (Global Ocean Associates, 2004); this remains to be verified by observations.

Leaving complicating factors of the Kuroshio aside, the west ridge itself is also capable of modifying internal tides, internal bores and internal solitary waves in two ways. First, it presents a partial physical barrier to the incoming internal waves from the east ridge. Second, it can also generate some internal waves that may add constructively to the westward propagation. Weighing these two competing factors, whether the west ridge reinforces or dampens the transmission of westward propagating internal waves is intuitively unclear.

The objective of this study is to evaluate the west ridge of the Luzon Strait as an internal wave mediator, using a fine-resolution hydrostatic model and a process-oriented nonhydrostatic model. By definition, a hydrostatic model disallows internal wave dispersion and therefore cannot produce internal solitary waves. Further, the resolution of the regional ocean model is too coarse to resolve internal solitary waves. Nevertheless, the hydrostatic model captures early phases of transition from internal tides to internal solitary waves. As we demonstrate below, this enables the hydrostatic model to reproduce the location and timing of internal solitary waves in the northern South China Sea as revealed by satellite images and in-situ observations. The nonhydrostatic model is used mainly to resolve internal solitary waves. With such fine resolution, it is incapable of accommodating large scale features such as the Kuroshio. Nevertheless, it provides useful diagnoses to collaborate with findings from the hydrostatic model.

2. Hydrostatic Simulations

We use the Ocean Nowcast/Forecast System (ONFS) of the Naval Research Laboratory to facilitate the study. The model domain (Fig. 4) covers the northern South China Sea, the Luzon Strait and a portion of the western Pacific Ocean with a horizontal resolution of 2.3 km. In terms of vertical resolution, there are 11 σ-layers in the top 147 m and 29 z-layers below. The ONFS system derives its ocean bottom topography from the Digital Bathymetry Data Base in 2-minute (DBDB2). Open boundary conditions are derived from a larger scale ONFS for the entire East China Sea (Ko *et al*., 2007). The Oregon State University (OSU) tidal forcing drives the tidal

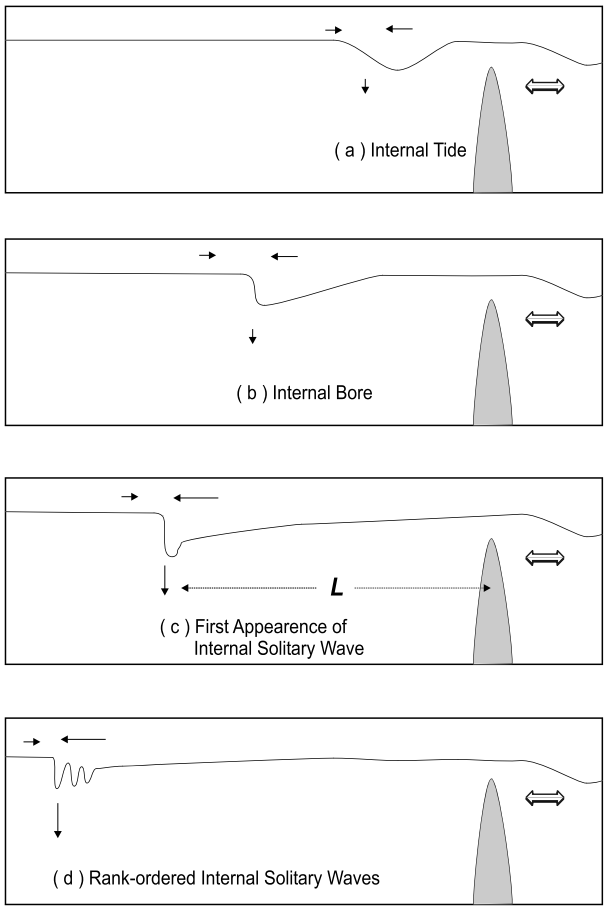

Fig. 3. Nonlinear transformation from barotropic tide to internal solitary waves by a ridge: (a) ridge-induced linear internal tide; (b) subsequent transformation to internal bore through nonlinear wave steepening; (c) first appearance of soliton-like feature; and (d) final emergence of rank-ordered solitary waves if the incoming tide is too strong or the ridge is too tall.

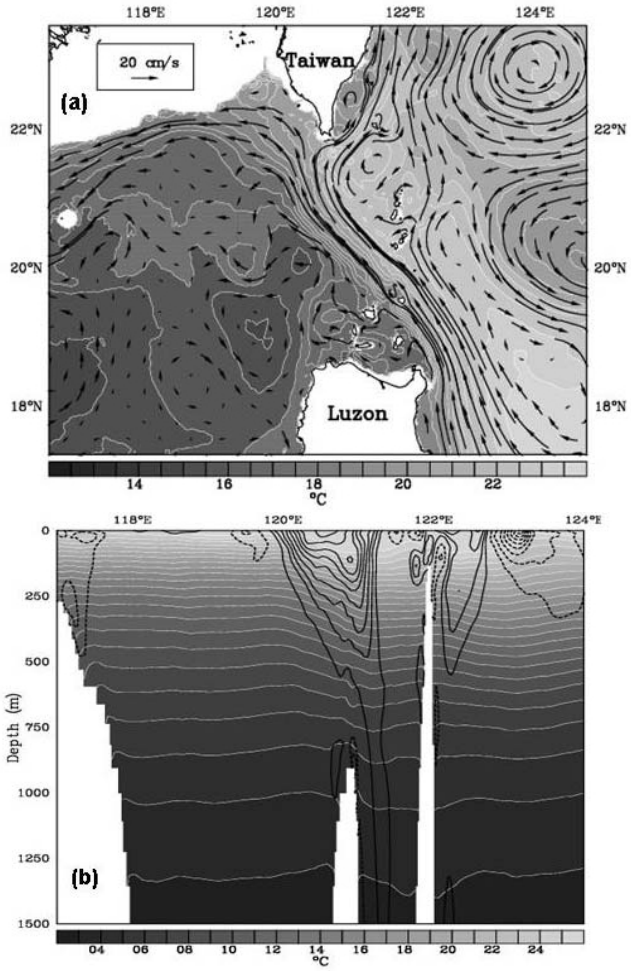

Fig. 4. (a) Model-produced potential temperature and flow fields at 150 m depth in the vicinity of Luzon Strait at 12:00 GMT, April 28, 2005, after filtering out high-frequency signals by a 48-hour low-pass filter. (b) Corresponding zonal section of potential temperature and meridional flow at 21°N. Northward and southward currents are contoured by solid and dashed lines, respectively, at intervals of 10 cm s^{-1}.

currents. A global weather forecast model (Navy Operational Global Atmospheric Prediction System or NOGAPS) and a regional weather forecast model (Coupled Ocean/Atmosphere Mesoscale Prediction System or COAMPS) provide the ocean surface forcing. The Ocean Nowcast/Forecast System also assimilates satellite altimeter data and Multi-Channel Sea Surface Temperature (MCSST) from satellite-derived AVHRR to further improve accuracy.

We use the ONFS to assess the effect of west ridge on wave formation in a realistic setting. In addition to the main experiment, which simulates the realistic setting, we also reduce the west ridge height by 20 percent in a parallel experiment. The area of west ridge height reduction is shown in Fig. 1(a). The strategy was to reduce the west ridge height sufficiently to induce visible changes in internal wave behaviors while minimizing changes in the Kuroshio, allowing us to assess the role of the west ridge alone. In this light, the 20 percent reduction turns out to be optimal.

Figure 5 shows the sea surface height at 05:00 GMT, April 29, 2005 produced by the ONFS. At this time there are three wave fronts, characterized by surface flow convergence and therefore sea surface elevation of varying strength, propagating westward from the Luzon Strait. Thick white curves are corresponding surface signatures of internal solitary waves inferred from a contemporaneous MODIS satellite image (not shown). The modeled wave fronts agree with satellite-inferred fronts reasonably well, even though the ONFS lacks horizontal reso-

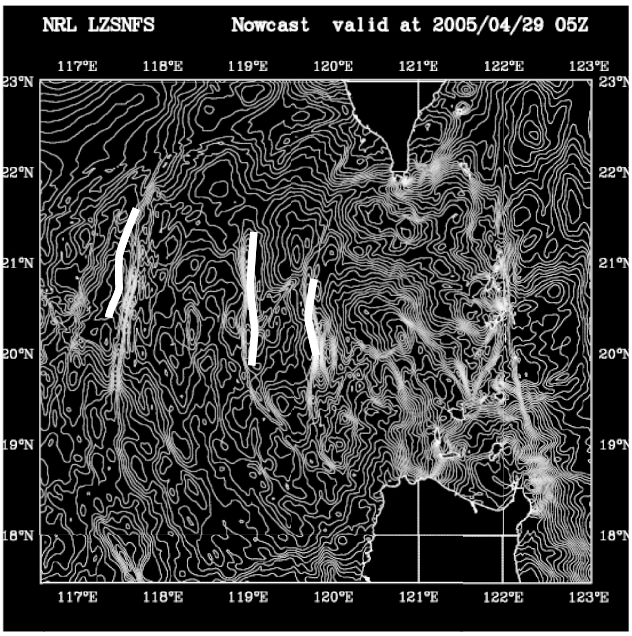

Fig. 5. Model-produced sea surface height at 05:00 GMT, April 29, 2005. Contour interval for the sea surface height is 2 cm. Thick white lines are locations of internal solitary waves inferred from a contemporaneous MODIS image.

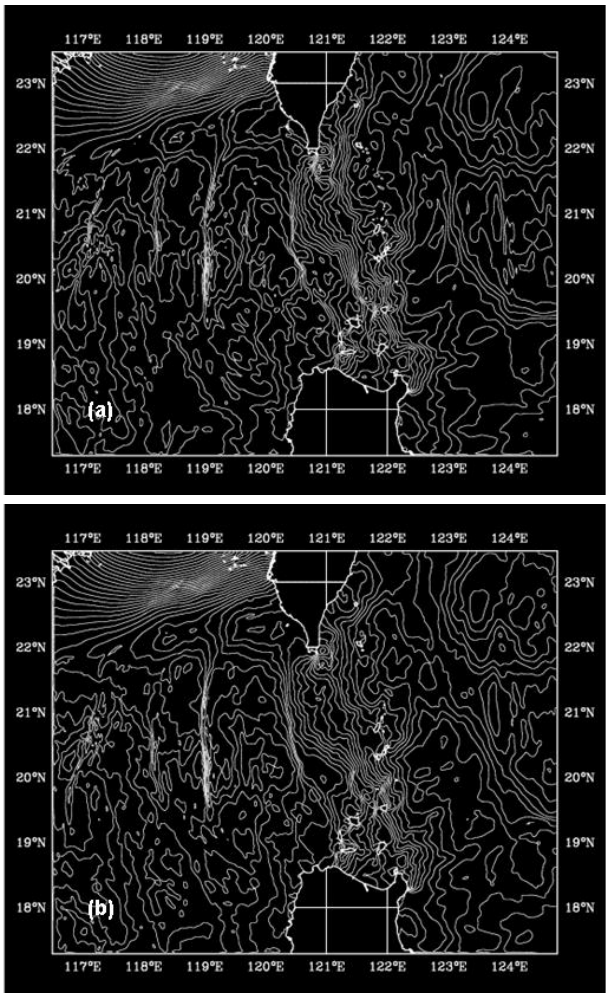

Fig. 6. (a) Model-produced temperature field at 150 m depth (12:00 GMT, April 28, 2005) with no ridge height reduction. (b) Corresponding plot with 20% reduction of west ridge height.

lution and nonhydrostatic dynamics to produce internal solitary waves.

Figure 6(a) shows the model-produced temperature field at 150 m depth at 12:00 GMT, April 28, 2005, while Fig. 6(b) shows the corresponding feature with the west ridge height (in the inserted rectangle in Fig. 1(a)) reduced by 20 percent. Westward propagating wave fronts manifest densely packed, north-south running isotherms. Judging from the zonal temperature gradient, the wave front at about 119°E appears to be the most prominent. With and without the west ridge height reduction, the Kuroshio front distribution changes little and the difference in wave fronts is subtle. One could argue, with substantial subjectivity, that the signals are slightly stronger if the west ridge height is reduced (Fig. 6(b)). This requires further confirmation, which is explored below.

Figure 7 shows corresponding temperature sections along 21°N with and without west ridge height reduction. At issue are waves located sufficiently to the west after they have adjusted fully to the impact of west ridge. Focusing on the most prominent deep-ocean wave front at about 119°E, the west ridge height reduction in Fig. 7(b) leads to deeper and narrower isotherm depression. West of 118°E (near the western model boundary), a wave front is significantly amplified by the shoaling continental slope. In this case, the west ridge height reduction in Fig. 7(b) leads to much deeper, but not necessarily narrower, isotherm depression. Apparently, a reduced west ridge height allows the incoming internal wave to pass by with less attenuation; thereafter the transmitted wave develops better into a sharper wave front through nonlinear wave steepening.

Figure 8 shows corresponding zonal velocity sections along 21°N. Zonal currents extend deeper between two ridges, in keeping with the deep Kuroshio Current. West of the Luzon Strait, zonal currents are mostly surface-trapped. An alternate series of westward and eastward velocity cores propagates westward from the Luzon Strait with a wavelength exceeding 100 km. The vertical and horizontal scales indicate the predominance of first-mode internal tides. With or without the ridge height reduction, the patterns are similar. In the deep ocean west of the Luzon Strait, the height reduction of west ridge (Fig. 8(b))

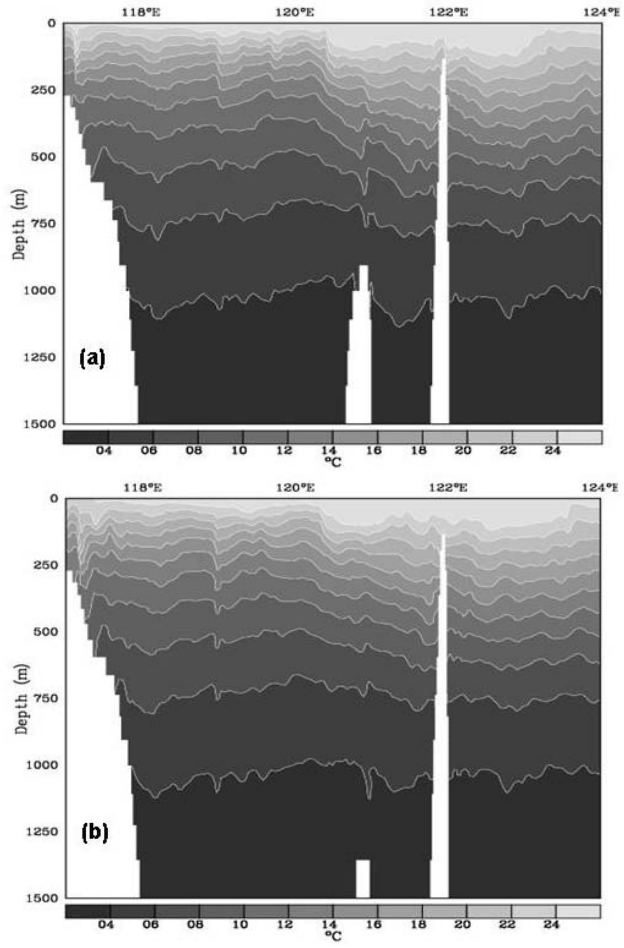

Fig. 7. (a) Model-produced zonal section of potential temperature at 21°N (12:00 GMT, April 28, 2005) without ridge height reduction. (b) Corresponding zonal section with 20% reduction of west ridge height.

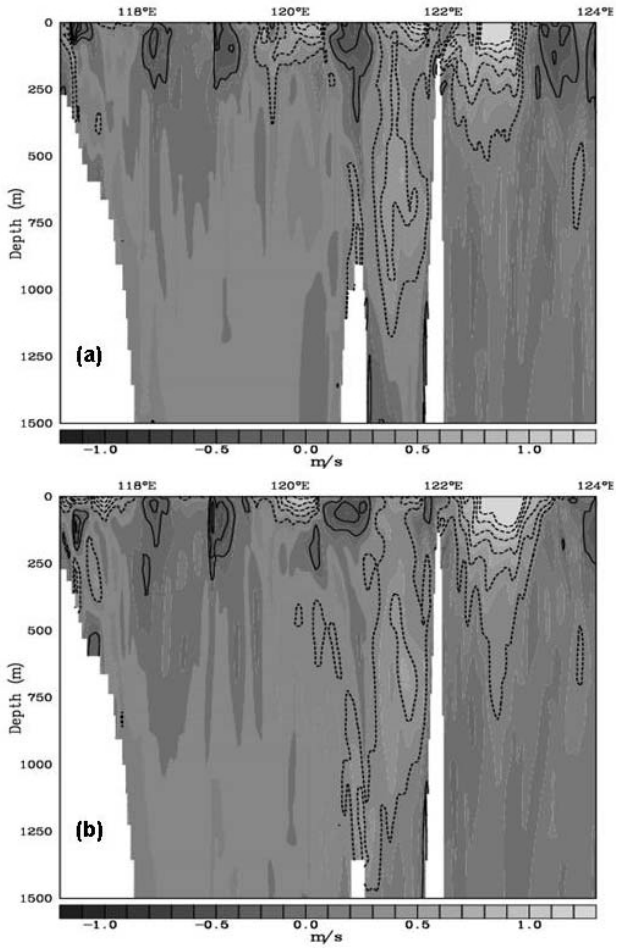

Fig. 8. (a) Model-produced zonal section of zonal flow at 21°N (12:00 GMT, April 28, 2005) without ridge reduction. (b) Corresponding zonal section with 20% reduction of west ridge height. Solid and broken contours indicate westward and eastward velocities with a contour interval of 20 cm s^{-1}.

generally leads to stronger and shallower internal tidal currents near the surface. Focusing on the most prominent deep-ocean wave front at about 119°E, the west ridge height reduction in Fig. 8(b) apparently strengthens the westward surface current behind the wave front. Thus, all indications seemingly suggest stronger wave fronts propagating westward if the west ridge height is reduced.

Without ridge height reduction, Fig. 9 shows model-produced upper 900 m isotherms at 119°E and 21°N from April 25 to May 2 of 2005. Large depressions arrive diurnally, with weaker semidiurnal waves in between. Hydrostatic approximation and coarse horizontal resolution prevent large depressions from evolving further into solitary waves. Nevertheless, these large depressions retain structures similar to that of internal solitary waves.

The foregoing instantaneous snapshots are far from being conclusive. To quantify further, Fig. 10 shows the depth-integrated zonal energy flux of internal tides, including both semidiurnal and diurnal components, with and without the west ridge height reduction. Following Nash *et al*. (2005), we compute the energy flux as

$$F = \int \langle p'u' \rangle dz, \tag{1}$$

where p' and u' are baroclinic pressure and zonal baroclinic velocity within a tidal frequency band, and the angle bracket denotes time averaging over 14 days. The semidiurnal and diurnal frequency bands are defined as 0.06–0.1 cycles per hour, and 0.03–0.05 cycles per hour, respectively. Pressure is computed from the model density field assuming hydrostatic balance.

For the semidiurnal internal tides (Fig. 10(a)), the major source of internal tides comes from the east ridge

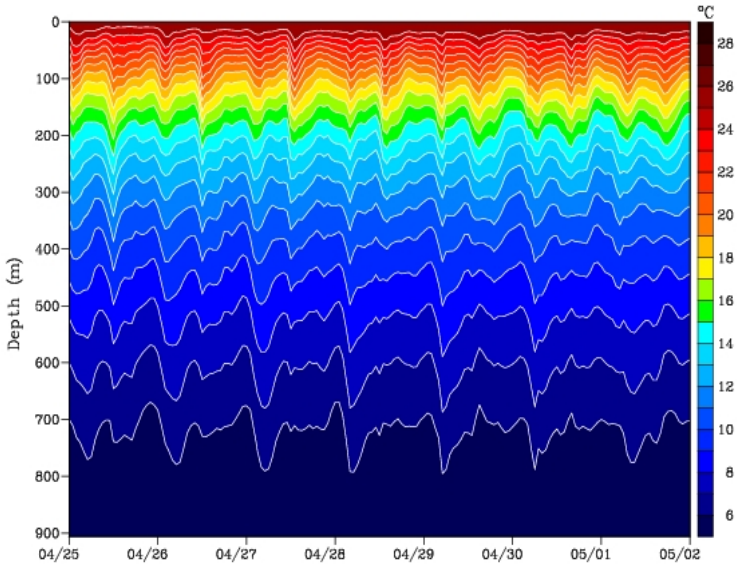

Fig. 9. Model-produced temperature time series without ridge height reduction at 21°N and 119°E from April 25 to May 2 of 2005.

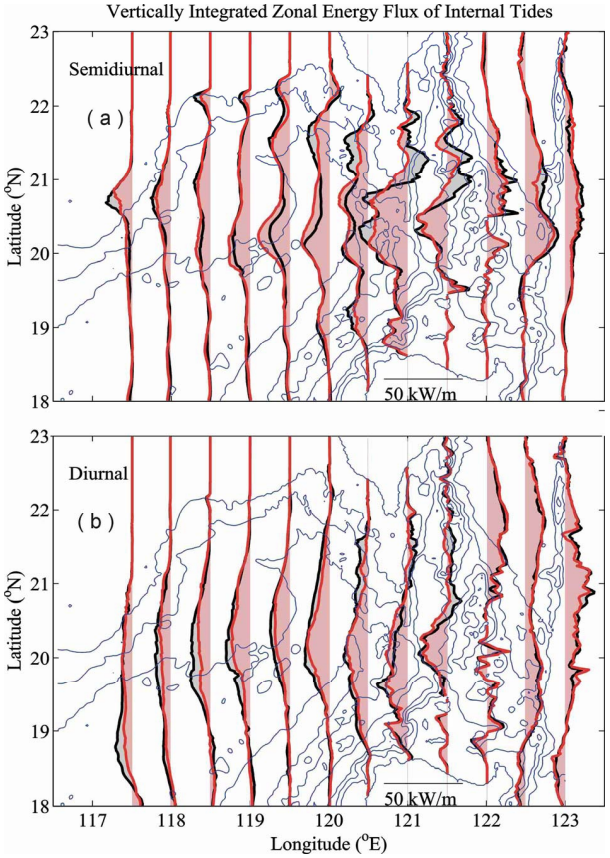

Fig. 10. Depth-integrated zonal energy fluxes of internal tides for (a) semidiurnal component and (b) diurnal component. Red and black correspond to results with and without west ridge height reduction, respectively. The contour interval for water depth is 1000 m.

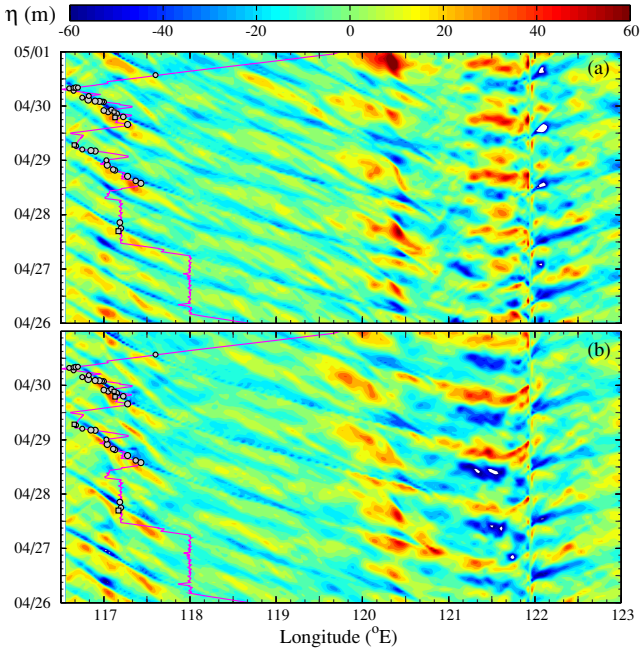

Fig. 11. (a) Zonal-temporal section of vertical isotherm displacements at 103 m depth along 21°N between April 26 and May 1 in 2005 predicted by the hydrostatic model. Red zigzag lines represent contemporaneous ship tracks. Grey filled symbols represent shipboard observations of internal solitary waves with amplitudes in excess of 100 m. Symbol size corresponds to the amplitude of internal solitary waves. (b) Corresponding section with 20% reduction of west ridge height.

in the middle reaches of the Luzon Strait between 19.5 and 20.5°N, where the depth-integrated internal energy flux diverges. Following this beam of energy westward into the deep northern South China Sea, the height reduction of the west ridge leads to, on average, larger westward internal energy flux. The enhancement is most visible at 119.5°E. This result points to the west ridge in the middle portion of the Luzon Strait as an energy blocker for the incoming internal tides from the east ridge. Although the west ridge in the middle reaches of the Luzon Strait could conceivably generate some semidiurnal internal tides by itself, this unknown amount of internal tide energy does not overcome the damping effect exerted by the west ridge. Moving farther westward onto the continental shelf, the west ridge height reduction does not necessarily lead to larger westward internal energy flux. This inconsistency is understandable, as internal tide dissipation over the shallow shelf introduces additional uncertainties in assessing the effect of west ridge height on internal tide propagation.

Model results indicate the northern shallow reaches of the west ridge as another generation site for the semidiurnal internal tides (Fig. 10(a)). West of 120°E, the two energy beams of semidiurnal internal tides are comparable in magnitude and meridional scale. Following the northern beam of energy westward, the height reduction of the west ridge actually reduces the westward internal energy flux. This is also understandable, as a lower ridge normally reduces the generation of internal tides.

For the diurnal internal tides (Fig. 10(b)), the major source of internal tides also comes from the east ridge in the middle reaches of the Luzon Strait where the depth-integrated internal energy flux diverges. Following this beam of energy westward, the height reduction of the west ridge actually reduces the westward energy flux. Although the west ridge is a physical barrier to incoming internal tides from the east ridge, it also generates some internal tides that apparently add constructively to the westward transmission to overcome the west ridge damping effect. In contrast to the semidiurnal internal tides, the northern shallow portion of the west ridge does not generate diurnal internal tides (Fig. 10(b)).

To further validate ONFS results by concurrent ship observations along 21°N (Lien, private communication), Fig. 11 shows zonal-temporal sections of vertical isotherm displacements at 103 m depth from April 26 to May 1 in 2005. Upper (a) and lower (b) panels are model results without and with west ridge height reduction, respectively. Zigzag lines in red are contemporaneous ship tracks with dots representing observed internal solitary waves with amplitudes greater than 100 m. The shipboard observations bear out the ONFS results reasonably well. The level of agreement is visually indistinguishable with or without the west ridge height reduction. The west ridge east of 120°E also excites a large isotherm elevation (red-orange spots) between each pair of westward transmissions of isotherm depressions (blue-green spots), but elevation signals appear to be localized as they do not move far westward. Over the continental shelf west of 118°E, internal tides arrive semi-daily with alternate strengths, apparently modulated by a diurnal beat. They also amplify and decelerate over the shoaling ocean bottom, in keeping with theoretical expectations.

3. Nonhydrostatic Simulations

The three-dimensional nonhydrostatic numerical model of Shaw and Chao (2006) is used below. The model is formulated under Boussinesq and rigid-lid approximations, and solves for three-dimensional velocity vector (u, v, w) in the eastward, northward and vertically upward directions, and the perturbation density (ρ) about a reference seawater density (ρ_0 = 1022 kg m^{-3}). The Coriolis parameter (f) is fixed at 20°N. The horizontal eddy viscosity and diffusivity are 4×10^4 cm^{2}s^{-1}. The vertical viscosity and diffusivity are 1 cm^{2}s^{-1} and 0.1 cm^{2}s^{-1}, respectively.

The model uses the Arakawa-C grid system, and spatial derivatives are center differenced to second-order accuracy. Vertical discretization follows a z-coordinate formulation. The horizontal and vertical resolutions are 250 m and 30 m, respectively. The time step is 30 s. On east and west open boundaries, waves are allowed to propagate through with an appropriate phase speed without reflection. Zero normal gradients for horizontal velocities and perturbation density are enforced at the ocean surface. No-slip boundary conditions for horizontal velocities and a zero normal gradient for the perturbation density are applied at the ocean bottom.

The model has been used mostly to study the three-dimensional aspects of the internal solitary wave propagation (Chao and Shaw, 2006). In the present application, it is rendered two-dimensional by disallowing variations in the meridional (y) direction. Figure 12 shows two model domains to be used below. In single-ridge experiments (Fig. 12(a)), the water depth over the ridge is

$$h(x) = -3000m + \frac{h_m}{1+\left[\left(x - x_m\right)/l_m\right]^2}. \qquad (2)$$

Unless otherwise stated, we choose x_m = 0 and l_m = 10 km. The ridge height (h_m) is 1800 m in Fig. 12(a), but can be changed in each experiment. The ridge topography is truncated at $3l_m$ away from the peak, so that the ridge width is $6l_m$. In double-ridge experiments (Fig. 12(b)), both ridges have the same analytical form as in single-ridge experiments. The peak-to-peak distance between two ridges is 120 km. The peak height (h_m) is 2600 m for

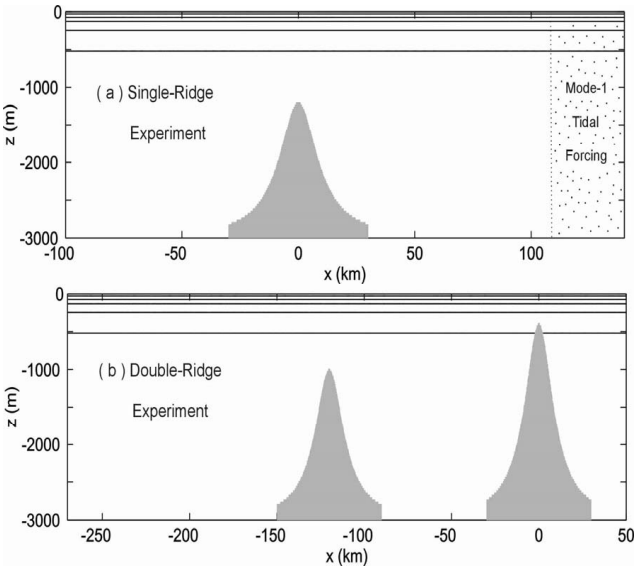

Fig. 12. Model domains of nonhydrostatic simulations with (a) a single ridge and (b) two ridges. For single-ridge experiments (a), stippling indicates the primary region containing a tidal generating force that produces westward progressive tide of the first baroclinic mode. For double-ridge experiments (b), the incoming tide is barotropic and enters the domain from the eastern boundary.

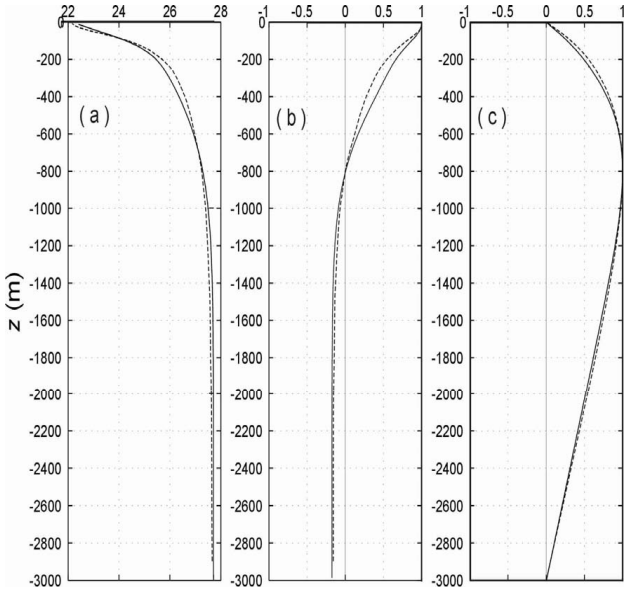

Fig. 13. Initial σ_θ profile in kg m^{-3} (a), first baroclinic modal structure for horizontal current (b), and first baroclinic model structure for vertical velocity or density (c). Dashed lines are derived from Levitus climatology between west and east ridges of the Luzon Strait (20°N, 117°E); solid lines are analytical fits.

the east ridge and 2000 m for the west ridge in Fig. 12(b). However, the height of the west ridge changes in each experiment.

Our preliminary experiments indicated that the model is not sensitive to the topographic profiles of ridges. Rather, it is sensitive to the ridge peak depth relative to the nodal depth of the first baroclinic mode profile. Figure 13 shows the typical potential density profile between two ridges (Fig. 13(a)), mode-1 profile for the horizontal currents (Fig. 13(b)), and mode-1 profile for the vertical velocity or density (Fig. 13(c)). Dashed lines are derived from Levitus climatology; solid lines are derived from analytically fitted perturbation density profile given by

$$\rho_b(z) = -\frac{\Delta\rho_1}{2}\left[1+\tanh\left(\frac{z-z_1}{D_1}\right)\right] - \frac{\Delta\rho_2}{2}\left[1+\tanh\left(\frac{z-z_2}{D_2}\right)\right], \quad (3)$$

which is used as initial perturbation density in the model. The optimum fit leads to $\Delta\rho_1$ = 4.2 kg m^{-3}, z_1 = –200 m, D_1 = 550 m, $\Delta\rho_2$ = 3.8 kg m^{-3}, z_2 = –50 m and D_2 = 100 m. For both climatology and the analytical fit, the nodal depth for horizontal currents is 800 m. The phase speed for the first baroclinic mode (c_1) is 2.52 m s^{-1} for the climatologic stratification and 2.7 m s^{-1} for the analytical fit. At semidiurnal frequency (ω), the wavelength for mode-1 internal tide,

$$\lambda_1 = 2\pi c_1 \Big/ \sqrt{\omega^2 - f^2}\,, \quad (4)$$

is 120 km for the climatologic stratification and 129 km for the analytical fit; both are comparable to the peak-to-peak distance between two ridges in the model (120 km).

Although our experiments cover a wide range of parameter space including ridge height, ridge shape, separation distance between two ridges, tidal frequency and Coriolis parameter, Table 1 lists only six experiments to be discussed at some length below. Experiments 1–3 summarize how a single ridge such as the west ridge of the Luzon Strait affects incoming internal waves. Experiments 4–6 reassess the role of the west ridge in a double-ridge setting.

3.1 Single-ridge experiments

If one regards the two ridges as being sufficiently far apart, the west ridge can be perceived as a distant passive receiver of incoming internal waves generated by the east ridge. Depending on the tidal strength, incoming waves can be internal tides, internal bores or internal solitary waves. For incoming internal tides of the first baroclinic mode, the west ridge will always dampen their

Table 1. List of experiments.

Experiment	Ridge	West ridge peak depth (m)	East ridge peak depth (m)	Mode-1 tidal forcing (a_0, m s^{-2})	Barotropic tidal speed (u_0, cm s^{-1})
1	none	—	—	1.5×10^{-4}	—
2	single	1200	—	1.5×10^{-4}	—
3	single	700	—	1.5×10^{-4}	—
4	single	—	400	—	7
5	double	1000	400	—	7
6	double	400	400	—	7

westward transmission. This is a foregone conclusion reached by Johnston and Merrifield (2003) using a hydrostatic model in a deep ocean setting similar to the present one. The amount and nature of damping are sensitive to the ridge slope and hence ridge height. The slope of an M_2 internal tidal wave characteristic is

$$s(z) = \sqrt{\frac{\omega^2 - f^2}{N(z)^2 - \omega^2}}, \qquad (5)$$

where $N(z)^2$ is the Brunt-Väisälä frequency. The ridge slope [$\alpha(z)$] is supercritical if $\alpha > s$ over a portion of the slope, near-critical if $\alpha \approx s$ at a certain depth, and subcritical if $\alpha < s$ everywhere. With sub-critical or near-critical ridges, damping is modest and arises mainly from energy transfer to higher baroclinic modes and dissipation. With supercritical ridges, damping increases dramatically mainly due to wave reflection by the ridge. The slope of a ridge also determines the conversion of internal tides into higher modes in the lee of the ridge (Müller and Liu, 2000). Since internal tides of the first baroclinic mode are dampened, further nonlinear transformation into internal solitary waves west of the ridge will also weaken. In light of extensive coverage by Johnston and Merrifield (2003), our experiments below preclude cases with incoming waves as internal tides.

What remains to be investigated is how a single ridge affects the transmission of internal bores and internal solitary waves. As it turns out, the ridge damping is not only for internal tides, but also includes internal bores and internal solitary waves. This is demonstrated below. As depicted in Fig. 12(a), a mode-1 M_2 tidal forcing is used to generate progressive tidal waves propagating westward toward the single ridge. Mathematically, a body force (F) is imposed in the x-momentum equation as

$$F(x,z,t) = a_1 \sin\left[k\left(x - x_0 + c_1 t\right)\right]\phi_1(z)\exp\left[k_i\left(x - x_0\right)\right], \qquad (6)$$

where $a_1 = 1.5 \times 10^{-4}$ m s^{-2} is the amplitude, $x_0 = 140$ km is the eastern boundary of the domain, $k = \sqrt{\omega^2 - f^2}\,/c_1$ and $\phi_1(z)$ the mode-1 profile for horizontal currents as shown in Fig. 13(b). Excluding the last term on the right side, Eq. (6) is resonant forcing for the first mode internal tides. To offset unlimited growth of internal tides in time, the tidal forcing is subject to spatial decay away from the eastern boundary with an e-folding scale of 30 km, so that $k_i = (30\ \text{km})^{-1}$. Setting up the forcing this way, the amplitude (a_1) dictates whether incoming waves are internal tides, internal bores or internal solitary waves. With our choice of a_1, the transition from internal bore to internal solitary wave occurs shortly before the wave approaches the ridge peak. Other choices of a_1 will nevertheless lead to the same conclusion that the ridge will always dampen regardless of the type of incoming waves.

Figure 14, from experiment 1 in Table 1, shows internal wave transformation without the ridge. At hour 16, an internal bore is in the process of forming at $x = 35$ km (Fig. 14(a)). Further transformation changes the bore to a packet of rank-ordered internal solitary waves as it propagates westward (Figs. 14(b), (c), (d)). If the internal tidal forcing is weaker, the end state can be a single solitary wave (results not shown). For the lead wave at hour 29 (Fig. 14(d)), the maximum westward and downward speeds are 213 cm s^{-1} and 32 cm s^{-1}, respectively. The corresponding maximum isopycnal depression is 217 m. The depression is admittedly too large, but will be reduced to realistic amplitudes after a ridge is imposed.

In experiment 2, a ridge extends to 1200 m below the sea surface. The ridge peak is well (400 m) below the nodal depth of the first baroclinic mode for horizontal currents (800 m); one expects modest damping by the ridge. Corresponding vertical snapshots (Fig. 15) shows little change in the transformation from internal bore to internal solitary wave as the wave approaches the ridge peak (Figs. 15(a) and (b)). Moving over to the west side of the ridge, the differential increase in water depth for each wave within the packet, and hence differential increase in phase speed, spreads out the packet of internal solitary waves. Since the lead wave attains greater propagation speeds for longer periods of time, however slightly,

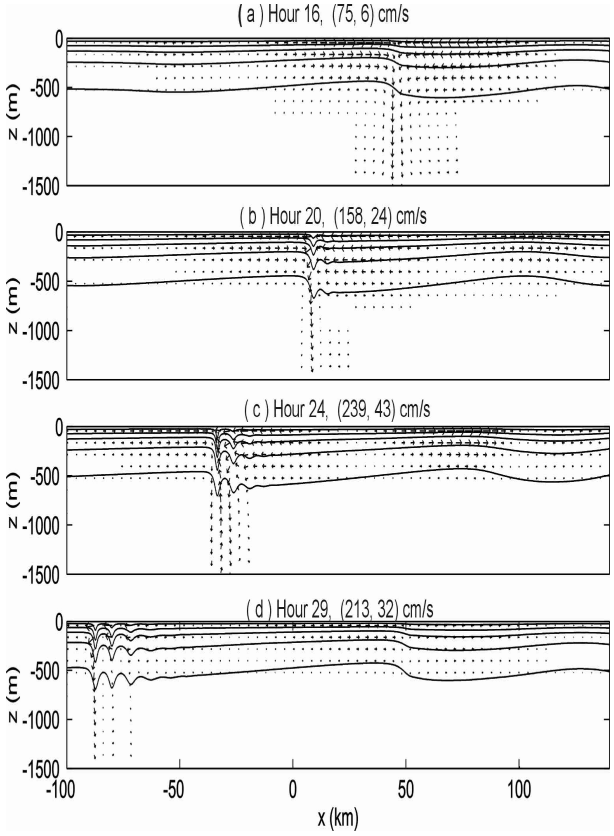

Fig. 14. Sequential vertical sections of zonal-vertical flow and potential density from experiment 1, showing the transformation from internal tide to internal solitary waves without a ridge. Contour interval for potential density is 1 kg m^{-3}. Maximum zonal and vertical speeds for the lead solitary wave are given at the top of each panel.

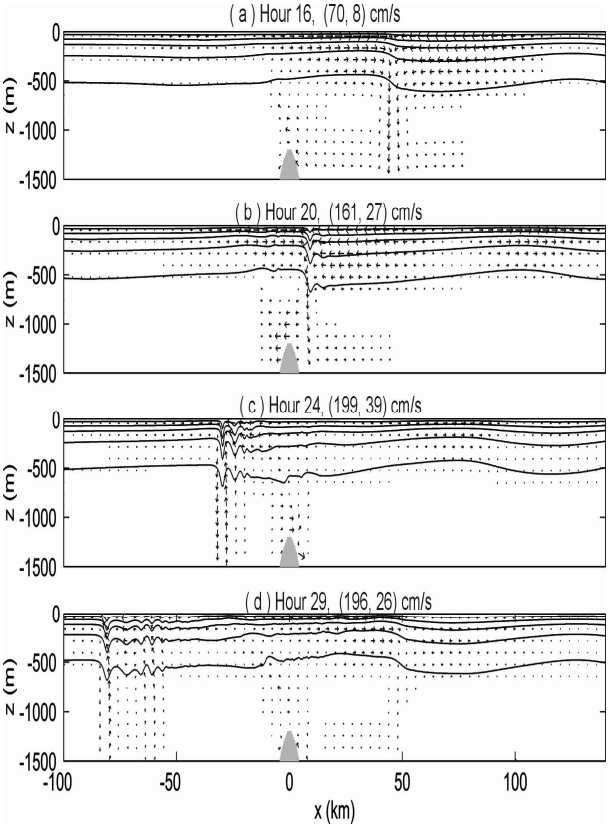

Fig. 15. As Fig. 14 except from experiment 2, which contains a ridge with its peak reaching 1200 m below sea surface. The internal solitary wave disintegrates and weakens after passing over the ridge.

it eventually leaves trailing waves behind and is in the process of becoming a single soliton (Fig. 15(d)). Thus differential propagation over the west side of the ridge appears to be the major damping factor for the transmitted wave. For the surviving lead wave at hour 29 (Fig. 15(d)), the maximum westward and downward speeds are 196 cm s^{-1} and 26 cm s^{-1}, respectively. The corresponding isopycnal depression is 203 m.

In Fig. 16 (experiment 3), the ridge height extends to 700 m below the sea surface or 100 m above the nodal depth of the first baroclinic mode for horizontal currents. Severe damping follows. After moving over to the west side of the ridge, the disintegration of the wave packet due to differential propagation becomes severe and the surviving lead solitary wave is considerably weaker (Fig. 16(d)). In addition, a reflection wave emerges on the east side of the ridge (Fig. 16(d)), further removing energy from the transmitted wave. At hour 29 (Fig. 16(d)), the maximum westward and downward speeds for the lead wave are 89 cm s^{-1} and 15 cm s^{-1}, respectively. The corresponding isopycnal depression is 114 m. If the ridge is even taller, the reflection wave will become even stronger at the expense of the transmitted wave. This quantitative aspect of the problem is not illustrated further.

For internal tides, the amount of wave transmission is sensitive to the ridge slope (Johnston and Merrifield, 2003). This sensitivity is lost if the incoming wave is transforming into an internal bore or internal solitary wave, even though the bore or internal solitary wave is embedded in each internal tidal wavelength and should be considered as part of an internal tidal wave. Instead, the transmission of internal bores or internal solitary waves is sensitive to the ridge peak depth relative to the nodal depth of the first baroclinic mode profile for horizontal currents. To verify this, Fig. 17 shows the transmitted wave strength as a function of ridge peak depth (H) and ridge width ($6l_m$). Without the ridge, the lead wave of the packet at hour 29 (Fig. 13(d)) is used as a reference. We use its maximum westward speed (u = 213 cm s^{-1}), maximum sinking speed (w = 32 cm s^{-1}) and maximum isopycnal depression (Δ = 217 m) as normali-

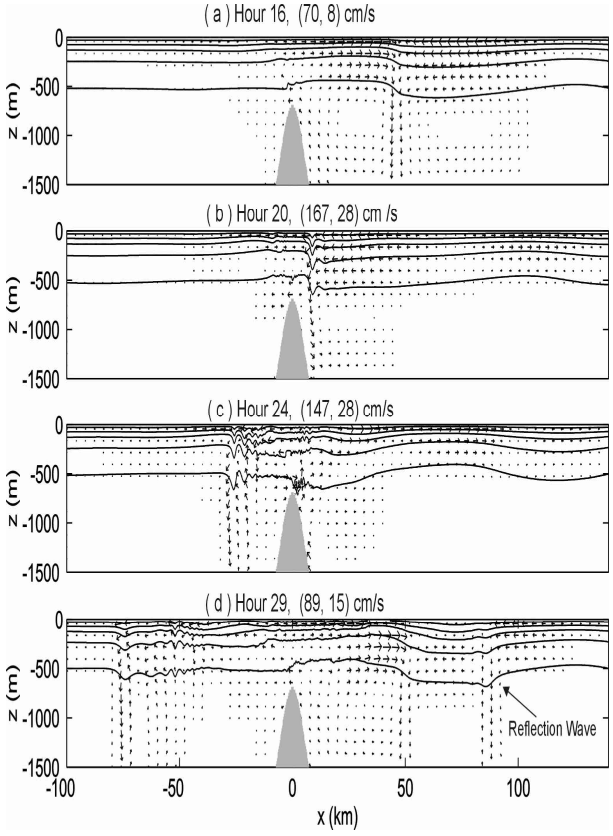

Fig. 16. As Fig. 14 except from experiment 3, which contains a ridge with its peak reaching 700 m below sea surface. The tall ridge reflects the incoming solitary wave and greatly dampens the transmitted wave.

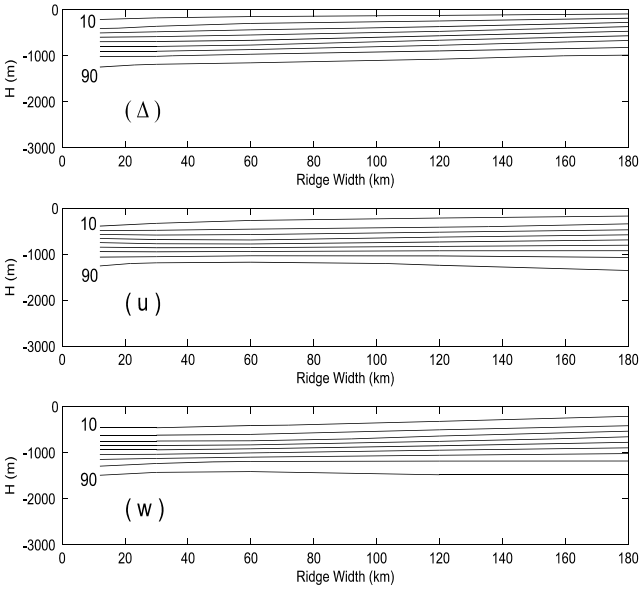

Fig. 17. Percentage of transmission for internal solitary waves passing over a single ridge as a function of ridge width and ridge peak depth (H). Maximum isopycnal depression (Δ), westward current speed (u) and downward speed (w) of the transmitted internal solitary wave are normalized by corresponding results without a ridge (Δ = 217 m, u = 213 cm s^{-1} and w = 32 cm s^{-1}). Contours for Δ, u and w are from 10% to 90% at intervals of 10%.

zation factors. After normalization, corresponding results at the same time and approximately the same location are expressed in percentage units.

Figure 17 shows little attenation of the transmitted wave strength if the ridge peak depth is well below the nodal depth (~800 m), but rapid attenuation as the ridge peak depth rises above the nodal depth. In contrast, the transmitted wave strength is insensitive to the ridge width and hence the critical ridge slope. Taking a ridge width of 60 km as an example, the ridge slope becomes supercritical for internal M_2 tides if the ridge peak depth rises above 1200 m depth. However, the transmitted wave strength shows no sensitivity to this criterion.

To put the width insensitivity issue in perspective, our range of ridge width variation (from 12 km to 180 km) is generous enough to cover normal width scales of the west ridge. In this range the bore or soliton transmission is insensitive to ridge width and hence to critical slope. However, if one widens a tall ridge further by orders of magnitude, the ridge peak then becomes a "continental shelf" for the incoming bore or soliton. In this wide ridge limit, severe attenuation results, even though the ridge slope becomes subcritical.

3.2 Double-ridge experiments

If one regards the separation distance between two ridges as insufficient, then the east ridge must be included. In this setting (Fig. 12(b)), the incoming tide is barotropic and imposed on the east boundary as $u = u_0 \sin\omega t$, where u_0 = 7 cm s^{-1}. The amplitude (u_0) and height of the east ridge dictate the strength of internal solitary waves and where an internal solitary wave will first appear. In the absence of the west ridge, our choices of u_0 and peak depth of the east ridge (400 m) produce an essentially single solitary wave that first appears some 175 km west of the ridge peak in every semidiurnal tidal cycle.

To establish a reference state, Fig. 18 (from experiment 4) shows the transformation from an internal tide to an internal soliton by the east ridge in the absence of the west ridge. At hour 12, the leading edge of the internal tide is around x = –65 km, characterized by visible downwelling motion (Fig. 18(a)). At hour 18, the tidal wave is in the process of becoming a bore around x = –120 km with much strengthened downwelling motion (Fig. 18(b)). The internal soliton fist appears around x = –175 km at hour 24 with even stronger downwelling mo-

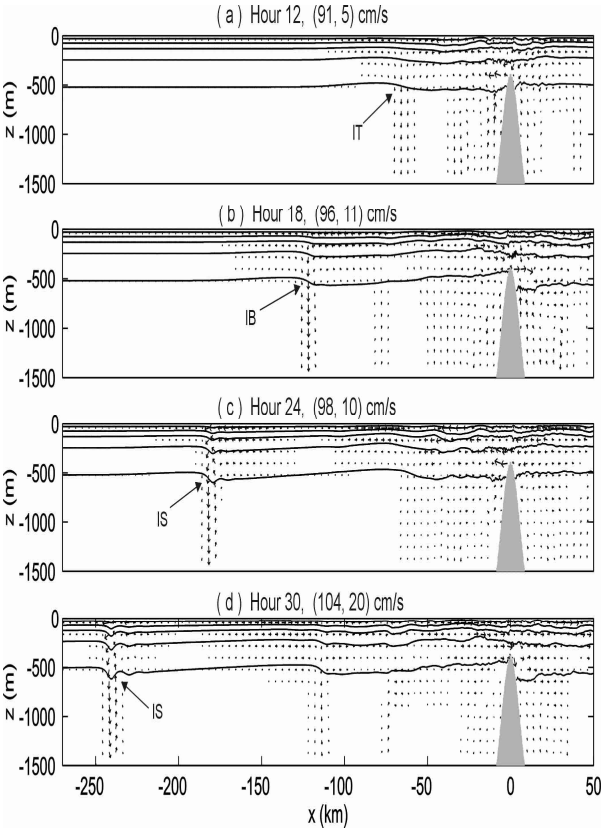

Fig. 18. Sequential vertical sections of zonal-vertical flow and potential density from experiment 4, showing barotropic tide over a tall ridge similar to the east ridge of the Luzon Strait and subsequent generation of internal tide (IT), internal bore (IB) and internal solitary wave (IS). Contour interval for potential density is 1 kg m^{-3}. Maximum zonal and vertical speeds are given at the top of each panel.

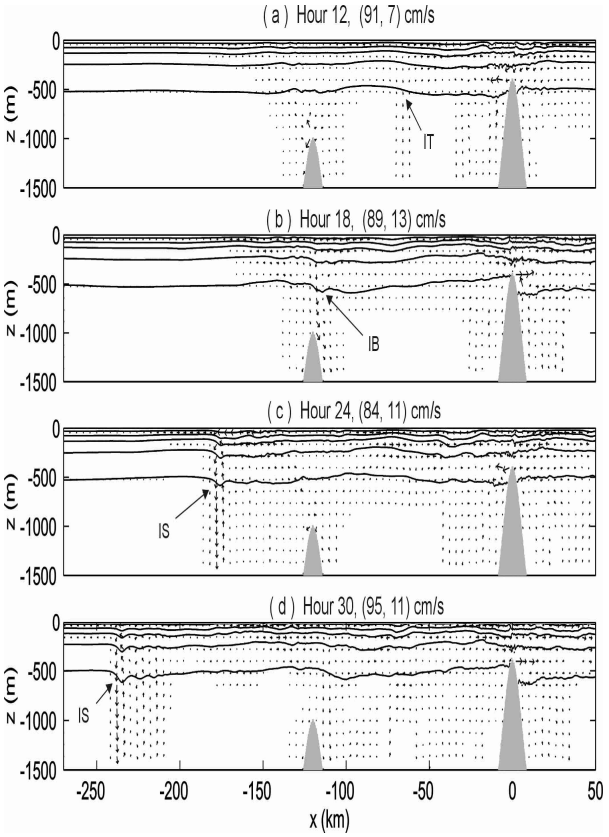

Fig. 19. As Fig. 18 except from experiment 5, to which a west ridge is added with its peak reaching 1000 m below sea surface.

tion at the leading edge (Fig. 18(c)), and reaches maturity at hour 30 and x = –240 km (Fig. 18(d)). The maximum westward and downward speeds are 94 cm s^{-1} and 9 cm s^{-1}, respectively, for the mature soliton. The corresponding maximum isopycnal depression is 118 m.

By including a west ridge with a peak depth of 1000 m in experiment 5, Fig. 19 shows consequent modifications. At hour 12, the west ridge has not exerted its influence on the incoming internal tide (Fig. 19(a)). Moving closer to the west ridge peak, the shoaling bottom depth accelerates the transformation from an internal tide to an internal bore (Fig. 19(b)). However, the premature development is not in phase and therefore does not help subsequent growth of an internal solitary wave further westward. By hour 30, the location of the mature soliton lagged slightly behind due to the earlier encounter with the west ridge (Fig. 19(d)); the characteristic maximum westward speed at sea surface (74 cm s^{-1}) and maximum downwelling speed at the leading edge (7 cm s^{-1}) for the soliton are more than 20 percent weaker as a result of west ridge modification. The corresponding maximum isopycnal depression of the soliton is 120 m.

Increasing the west ridge height further to a peak depth of 400 m below the sea surface, both ridges become equally imposing in experiment 6. This is a scenario comparable to the setting in the northern reaches of the Luzon Strait. Figure 20, from experiment 6, shows corresponding snapshots. Severe blocking by the west ridge to a large extent eliminates incoming internal tides from the east ridge. This can easily be seen by comparing surface currents in Fig. 20 with that in Fig. 18, which excludes the west ridge. Between two ridges, the west ridge greatly weakens the incoming surface currents as they approach the peak (Fig. 20). In this case, the west ridge becomes the primary wave maker, generating internal bores and internal solitary waves to its west at the semidiurnal frequency. At hour 18, an internal bore is formed at about x = –240 km (Fig. 20(b)). At hour 30, an internal solitary wave appears at about x = –235 km (Fig. 20(d)). Its maximum westward and downward speeds at the leading edge are 75 cm s^{-1} and 5 cm s^{-1}, respectively.

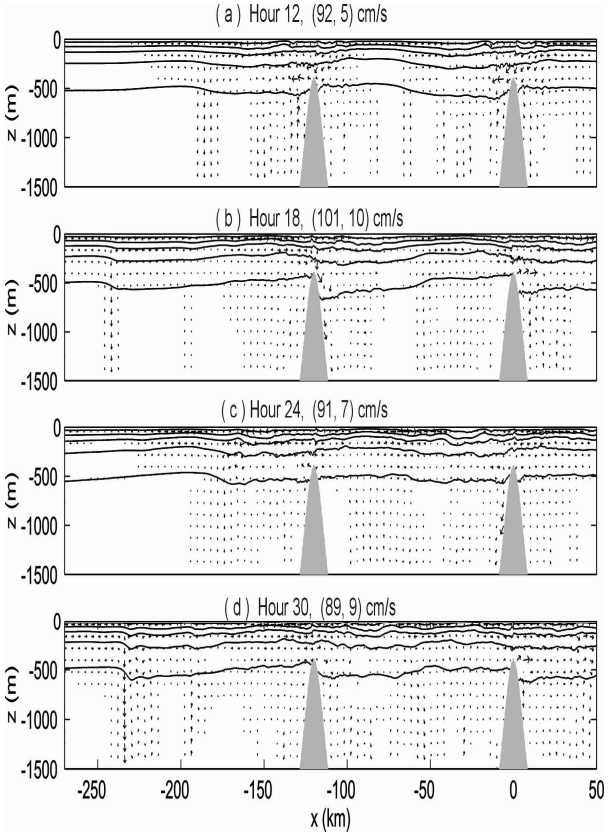

Fig. 20. As Fig. 18 except from experiment 6, to which a west ridge is added with its peak reaching 400 m below sea surface.

The maximum isopycnal depression for the soliton in Fig. 20(d) is 127 m.

3.3 Model sensitivity to other parameters

Other single- or double-ridge experiments are noted below without figures. Given the same tidal strength and ridge height, the transformation from diurnal internal tides to internal solitary waves takes, roughly speaking, twice the length of time and distance from the east ridge to complete, to the point that the zonal extent of the northern South China Sea may be inadequate to allow for the complete transformation. The Coriolis force normally diverts a little energy from zonal to meridional, thus making the internal tides, internal bores and internal solitary waves slightly weaker. The model is very insensitive to eddy viscosities, eddy diffusivities and bottom drag; a ten-fold increase, for example, brings about little visible change.

We have also varied ridge heights, ridge widths, ridge shapes and distance between two ridges. The possible combinations are virtually inexhaustible. Nevertheless, these numerical experiments, too numerous to be included here, failed to produce even one counterexample of the west ridge actually enhancing a transmitted internal wave.

4. Conclusions

Entering the Luzon Strait, a portion of the barotropic M_2 tides is blocked and converted to internal M_2 tides by the east ridge in the middle portion of the Strait (Niwa and Hibiya, 2004). Subsequent transformation to internal bores and internal solitary waves requires some propagation distance. Depending on the tidal strength, the west ridge at the receiving end may be approached by internal tides, internal bores or internal solitary waves. A hydrostatic nowcast/forecast system for the northern South China Sea and a nonhydrostatic process-oriented model are used to evaluate how the west ridge of Luzon Strait modifies westward propagation of these waves. The former model is all-inclusive, but is ill-suited to resolving fine-scale internal bores and internal solitary waves. The latter model overcomes this deficiency, but its fine grid size—necessary to cope with internal bores and internal solitary waves—precludes the possibility of including large-scale features such as the Kuroshio. In the hydrostatic nowcast/forecast system, the strategy taken is to reduce the height of the west ridge by a small amount to minimize changes in the Kuroshio strength and location. The height reduction of the west ridge leads to the amplification of nonlinear internal waves entering the northern South China Sea from the east ridge. The nonhydrostatic model employs a variety of ridge heights, widths, shapes and distance between two ridges. In all cases, the west ridge dampens the westward propagation of M_2 internal waves originating from the east ridge.

In assessing the west ridge's contribution to the M_2 internal wave field of the northern South China Sea, one must distinguish its deeper portion in the middle reaches of Luzon Strait from shallow reaches in the north. The west ridge in the middle reaches of Luzon Strait creates a deficit by dampening westward transmission of internal waves coming from the east ridge; its own generation of internal waves is inadequate to overcome the deficit. The northern, shallow portion of the west ridge is a generation site for internal tides on its own and therefore contributes positively to the internal wave field of the northern South China Sea.

The west ridge not only modifies the westward propagation of internal waves, but also provides an anchor for the shoaling thermocline associated with the Kuroshio. Theoretically, the rising thermocline can by itself be a source of internal solitary waves. The possible generation of internal solitary waves by the rising thermocline, if identified in the future, will be regarded by us as Kuroshio-induced. The west ridge serves an indirect role of partially locking the Kuroshio in place.

Leaving aside the uncertain complications created

by the Kuroshio front, the ridge reduction experiment in the presence of the Kuroshio points to the deeper portion of the west ridge in its present-day condition as a dampener of M_2 internal waves originated from the east ridge. Idealized nonhydrostatic experiments shed some lights on the dampening process. In particular, the west ridge in the middle reaches of the Luzon Strait hinders but does not annihilate the wave transmission because of its modest height. In the northern reaches of the Luzon Strait, the west ridge becomes imposing in height and generates westward propagating internal tides; this is evident in Fig. 1. Given enough lee time and distance, the internal tides generated by the northern portion of the west ridge, if strong enough, are potentially capable of transforming into internal bores or internal solitary waves before they reach the shallow Chinese continental shelf to the west. Whether or not this actually occurs is, to our knowledge, largely unknown and remains to be verified.

Acknowledgements

This work was supported by the U.S. Office of Naval Research, Code 322 PO under contracts N00014-05-1-0279, N00014-05WX-2-0647, N00014-04-1-0237 and N00014-05-1-0280.

References

Chao, S. Y. and P. T. Shaw (2006): Reflection and diffraction of internal solitary waves by a circular island. *J. Oceanogr.*, **52**, 811–823.

Global Ocean Associates (2004): *An Atlas of Internal Solitary-like Waves and Their Properties*. 2nd ed. (http://www.internal waveatlas.com/).

Johnston, T. M. S. and M. A. Merrifield (2003): Internal tide scattering at seamounts, ridges and islands. *J. Geophys. Res.*, **108**, doi:10.1029/2002JC001528.

Ko, D. S., P. J. Martin, C. D. Rowley and R. H. Preller (2007): A real-time coastal ocean prediction experiment for MREA04. *J. Mar. Syst.*, doi:10.1016/j.jmarsys.2007.02.022.

Liu, C.-T., R. Pinkel, M.-K. Hsu, J. M. Klymak, H.-W. Chen and C. Villanoy (2006): Nonlinear internal waves from the Luzon Strait. *EOS*, **87**, No. 42, 449–451.

Lynch, J. F., S. R. Ramp, C.-S. Chiu, T. Y. Tang, Y.-J. Yang and J. A. Simmen (2004): Research highlights from the Asian Seas International Acoustics Experiment in the South China Sea. *IEEE J. Oceanic Eng.*, **29**, 1067–1074.

Müller, P. and X. Liu (2000): Scattering of internal waves at finite topography in two dimensions: I. Theory and case studies. *J. Phys. Oceanogr.*, **30**, 532–549.

Nash, J. D., M. H. Alford and E. Kunze (2005): On estimating internal wave energy fluxes in the ocean. *J. Atmos. Oceanic Technol.*, **22**, 1551–1570.

Niwa, Y. and T. Hibiya (2004): Three-dimensional numerical simulation of M_2 internal tides in the East China Sea. *J. Geophys. Res.*, **109**, C04027, doi:10.1029/2003JC001923.

Shaw, P. T. and S. Y. Chao (2006): A nonhydrostatic primitive equation model for studying small-scale processes: an object-oriented approach. *Cont. Shelf Res.*, **26**, 1416–1432.

Yang, Y. J., T. Y. Tang, M. H. Chuang, A. K. Liu, M.-K. Hsu and S. R. Ramp (2004): Soliton northeast of Tung-Sha Island, Pilot study of ASIAEX. *IEEE J. Oceanic Eng.*, **29**, 1182–1199.

Zhao, Z., V. Klemas, Q. Zheng and X.-H. Yan (2004): Remote sensing evidence for baroclinic tide origin of internal solitary waves in the northeastern South China Sea. *Geophys. Res. Lett.*, **31**, doi:10.1029/2003GL019077.